Magnetotransport study of Dirac fermions in $YbMnBi_2$ antiferromagnet

Aifeng Wang (王爱峰),[1] I. Zaliznyak,[1] Weijun Ren (任卫军),[1,2] Lijun Wu,[1] D. Graf,[3] V. O. Garlea,[4] J. B. Warren,[5] E. Bozin,[1] Yimei Zhu,[1] and C. Petrovic[1]

[1]*Condensed Matter Physics and Materials Science Department, Brookhaven National Laboratory, Upton, New York 11973, USA*

[2]*Shenyang National Laboratory for Materials Science, Institute of Metal Research, Chinese Academy of Sciences, Shenyang 110016, China*

[3]*National High Magnetic Field Laboratory, Florida State University, Tallahassee, Florida 32306-4005, USA*

[4]*Quantum Condensed Matter Division, Oak Ridge National Laboratory, Oak Ridge, Tennessee 37831, USA*

[5]*Instrument Division, Brookhaven National Laboratory, Upton, New York 11973, USA*

(Received 1 April 2016; revised manuscript received 27 July 2016; published 24 October 2016)

We report quantum transport and Dirac fermions in $YbMnBi_2$ single crystals. $YbMnBi_2$ is a layered material with anisotropic conductivity and magnetic order below 290 K. Magnetotransport properties, nonzero Berry phase, and small cyclotron mass indicate the presence of Dirac fermions. Angular-dependent magnetoresistance indicates a possible quasi-two-dimensional Fermi surface, whereas the deviation from the nontrivial Berry phase expected for Dirac states suggests the contribution of parabolic bands at the Fermi level or spin-orbit coupling.

DOI: 10.1103/PhysRevB.94.165161

I. INTRODUCTION

The energy dispersion of carriers in Dirac materials can be approximated by the relativistic Dirac equation [1]. By now it has been established that Dirac states can be found in a wide range of materials, such as iron-based or copper-oxide superconductors, graphene, and topological insulators [2–9]. In the quantum limit, all carriers are condensed to the lowest Landau level (LL) [10]. This is easily realized in laboratory magnetic fields for Dirac fermions since the distance between the lowest and first LL of Dirac fermions is large, in contrast to the conventional electron gas with parabolic energy dispersion. In such a case, the components of the resistivity tensor ρ_{xx} and ρ_{xy} are linear in the magnetic field [11]; the quantum Hall effect, nontrivial Berry phase, and large unsaturated linear magnetoresistance (MR) are observed [5,12–14].

Crystals with quasi-two-dimensional (quasi-2D) bismuth layers such as $AMnBi_2$ (A = alkaline earth) have also been shown to host quasi-2D Dirac states similar to graphene and topological insulators [15–20]. The local arrangement of alkaline-earth atoms and spin-orbit coupling is rather important for the characteristics of Dirac cone states. In $SrMnBi_2$, the degeneracy along the band-crossing line is lifted, except at the place of anisotropic Dirac cone. In contrast, the energy eigenvalue difference due to the perturbation potential created by staggered alkaline-earth atoms results in a zero-energy line in momentum space in $CaMnBi_2$.

In the presence of the time-reversal or space-inversion symmetry breaking, the doubly degenerate Dirac point can split into a pair of Weyl nodes with opposite chirality [21–23]. Weyl semimetal signatures due to the space-inversion symmetry breaking have been observed in, for example, TaAs, NbAs, TaP, and NbP [24–27]. $YbMnBi_2$ is a material isostructural to $CaMnBi_2$, featuring magnetic order at similar temperatures [16,28]. Therefore, the observation of Weyl points and the connecting arc of surface states in $YbMnBi_2$ might be experimental evidence of a Weyl semimetal due to time-reversal symmetry breaking [28]. It is of interest to study quantum transport in $YbMnBi_2$. In this paper, we perform magnetoresistance measurements up to 35 T. The nonzero Berry phase, small cyclotron mass, and large mobility confirm the existence of Dirac fermions in Bi square nets. The quasi-2D in-plane magnetoresistance (MR) shows a crossover from parabolic-in-field semiclassical MR to high-field linear-in-field dependence. The temperature dependence of crossover field B^* is quadratic, as expected for Dirac fermions.

II. EXPERIMENTAL DETAILS

$YbMnBi_2$ single crystals were grown from excess Bi. Yb, Mn, and Bi were mixed together according to the ratio Yb:Mn:Bi = 1:1:10. Then, the mixture was placed into an alumina crucible, sealed in a quartz tube, heated slowly to 900 °C, kept at 900 °C for 2 h, and cooled to 400 °C, where the excess Bi flux was decanted. Shiny single crystals with typical size $3 \times 3 \times 1$ mm^3 can be obtained. The single crystals free of residual flux droplets can be obtained by cutting the six faces of the cuboid. The element analysis was performed using an energy-dispersive x-ray spectroscopy (EDX) in a JEOL LSM-6500 scanning electron microscope. Single-crystal neutron-diffraction measurements were performed using the HB3A four-circle diffractometer at the High Flux Isotope Reactor at Oak Ridge National Laboratory. A crystal specimen of approximately $2 \times 2 \times 1$ mm^3 was loaded in a closed-cycle refrigerator whose temperature was controlled in the range 4–350 K. For the measurements, we used a monochromatic beam with the wavelength 1.551 Å selected by a multilayer [110]-wafer silicon monochromator, and the scattered intensity was measured using an Anger-camera-type detector. The neutron-diffraction data were analyzed by using the FULLPROF SUITE package. A transmission-electron-microscopy (TEM) sample was prepared by crushing the single-crystal sample, and then dropping to a Lacey carbon grid. An x-ray powder-diffraction experiment was performed at the 28-ID-C beam line of NSLS-II at Brookhaven National Laboratory, and the data were collected on the pulverized sample in a cylindrical polyimide capillary by using a monochromatic beam with wavelength of 0.01858 nm and Perkin-Elmer image plate detector. Data integration to 2θ was carried out using FIT2D, while structural refinement of the $P4/nmm$ model used GSAS operated under the EXPGUI platform [29–31]. High-resolution TEM imaging and electron diffraction were performed using

the double aberration-corrected JEOL-ARM200CF microscope with a cold-field emission gun and operated at 200 kV. Magnetotransport measurements up to 9 T were conducted in a Quantum Design PPMS-9. Magnetotransport at high magnetic field up to 35 T was conducted at the National High Magnetic Field Laboratory (NHMFL) in Tallahassee. The transport measurements were performed on cleaved and polished single crystals. Polishing is necessary in order to remove residual bismuth droplets from the surface of as-grown single crystals. Electrical contacts used in resistivity measurements were put on the crystals using a standard four-probe configuration. Hall resistivity was measured by the four-terminal technique by switching the polarity of the magnetic field H//c to eliminate the contribution of ρ_{xx} due to the misalignment of the voltage contacts. The Hall resistivity is obtained by $\rho_{xy} = [V_{xy}(B) - V_{xy}(-B)] \times d/2I_{xx}$, where d is the thickness of the crystals, I_{xx} is the longitudinal current, $V_{xy}(B)$ is the transverse voltage of the positive field, and $V_{xy}(-B)$ is the negative field.

III. CRYSTAL AND MAGNETIC STRUCTURE

The crystal and magnetic structure of $YbMnBi_2$ determined by neutron diffraction and high-resolution TEM (HRTEM) is presented in Fig. 1. The nuclear lattice structure was determined from measurements at $T = 310$ K, where magnetic order is absent. The magnetic structure was determined at $T = 4$ K, and the refined saturated magnetic moment at this temperature is $4.3(1)\mu_B$/Mn. Refinements were carried out using data sets of 82 reflections; the resulting structural parameters are listed in Table I. R-factors ~5% were obtained for both temperatures. No indication of structural transformation between 300 and 4 K has been detected, and no orthorhombic or monoclinic distortions were observed within the HB3a wave-vector resolution. The data is fit equally well in both tetragonal and orthorhombic symmetry. The magnetic space group describing the antiferromagnetic (AFM) order at 4 K [Fig. 1(a)] can be refined in $P4'/n'm'm : (3/4,1/4,0|0,0,mz)(1/4,3/4,0|0,0,-mz)$. The scanning electron microscopy (SEM)-obtained atomic ratio of Yb:Mn:Bi is 26:26:48, consistent with the composition $YbMnBi_2$. Both HRTEM electron-diffraction pattern and fast Fourier transform can be well indexed as the (110)* zone of the $YbMnBi_2$ structure. Powder-diffraction data are well explained by the $P4/nmm$ model of $YbMnBi_2$ [$a = 4.488(2)$ Å, $c = 10.826(2)$ Å]; see Fig. 1(h). In addition to the main phase, about 10% by weight of the Bi_2O_3 phase was also observed due to secondary oxidation of unreacted Bi metal on a crystal surface during pulverization of the single-crystal specimen.

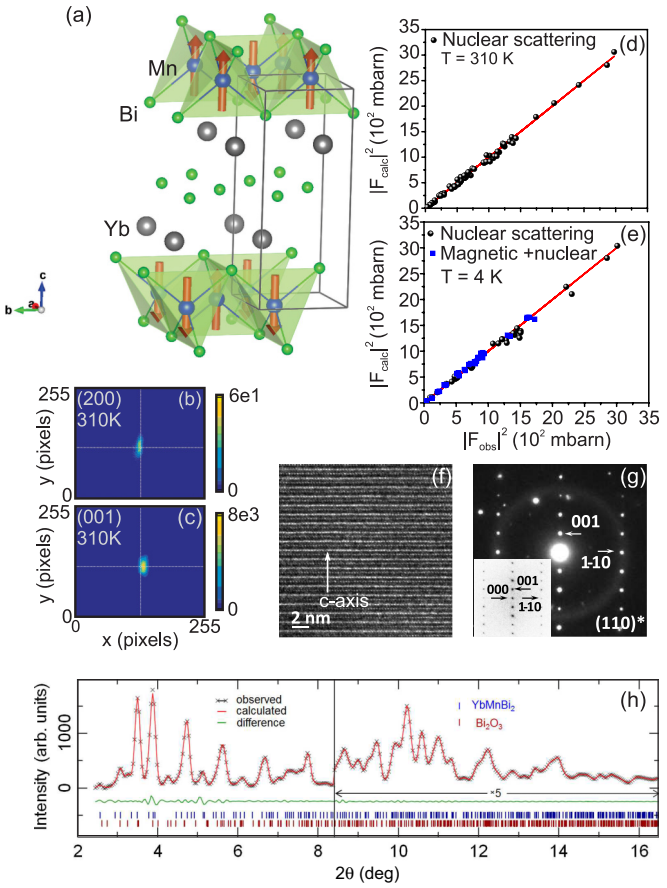

FIG. 1. (a) Crystal and magnetic structure of $YbMnBi_2$. Arrows show the ordered Mn magnetic moments, $\mu_{Mn} = 4.3(1)\mu_B$, refined at 4 K. The moments point along the c axis; the magnetic space group describing the AFM order is $P4'/n'm'm : (3/4,1/4,0|0,0,mz)(1/4,3/4,0|0,0,-mz)$. (b),(c) Neutron intensity patterns of (200) and (001) nuclear structural Bragg peaks, respectively, of a $YbMnBi_2$ single crystal on the two-dimensional position-sensitive detector on a HB3a diffractometer, indicating perfect crystalline structure. (d),(e) Summary of the structural refinement of $YbMnBi_2$ in the magnetically disordered phase at 310 K, and at 4 K where it is antiferromagnetically ordered. (f) High-resolution transmission electron microscopy (HRTEM) image and (g) corresponding electron diffraction pattern (EDP) viewed along the [110] direction. The inset in (g) is the FFT from the image shown in (f). (h) Structural refinement of powder-diffraction data. Ticks mark reflections, top row refers to the main phase, and bottom row refers to Bi_2O_3 due to sample preparation.

IV. RESULTS AND DISCUSSION

Figure 2(a) shows the temperature dependence of the in-plane (ρ_{ab}) and out-of-plane (ρ_c) resistivity at 0 and 9 T for a $YbMnBi_2$ single crystal. The in-plane resistivity becomes flat below 8 K, extrapolating to a residual resistivity $\rho_0(0\text{ T}) \approx 4.77\ \mu\Omega$ cm. The residual resistivity ratio (RRR) $\rho(300\text{ K})/\rho_0$ is about 20. The MR ratio, MR = $[\rho_{ab}(B)–\rho_{ab}(0)]$, is 234% at 2 K in a 9 T field. The MR is gradually suppressed with temperature increase. The resistivity is highly anisotropic. The hump below 300 K in $\rho_c(T)$ could indicate a crossover from high-T incoherent to low-T coherent conduction [32,33]. As shown in the inset in Fig. 2(a), ρ_{ab} is quadratic in temperature below about 5 K: $\rho(T) = \rho_0 + AT^2$ with $A = 5.74n\ \Omega\,\text{cm}\,\text{K}^{-2}$. The parameter A is inversely proportional to the Fermi temperature and is only one-third of that of $SrMnBi_2$ [17]. This indicates that the effective mass in $YbMnBi_2$ is rather small.

Specific-heat measurement on $YbMnBi_2$ is shown in Fig. 2(b). A peak is clearly observed at around 285 K, which could be attributed to the magnetic transition [34]. The fitting of the low-temperature data using $C_p = \gamma_n T + \beta T^3 + \eta T^5$ gives $\gamma_n = 2.16\ \text{mJ mol}^{-1}\,\text{K}^{-2}$, $\beta = 2.36\ \text{mJ mol}^{-1}\,\text{K}^{-4}$, and

TABLE I. The crystal and magnetic structure parameters of $YbMnBi_2$ determined by neutron diffraction. The refinement was carried out using 82 Bragg reflections measured on the HB3A diffractometer using a monochromatic neutron beam with wavelength $\lambda \approx 1.55$ Å. Each reflection was measured by performing the sample rotation (ω) scan to extract the integrated intensity.

$T = 310$ K					
Symmetry group: $P4/nmm$ Bragg R-factor: 5.25					
$a = b = 4.48(1)$, $c = 10.80(2)$ Magnetic moment $0\mu_B$/Mn.					
Atom	x	y	z	B_{iso}	Site multiplicity
Yb1	0.25	0.25	0.73174(19)	1.051(148)	2
Mn1	0.75	0.25	0.0	1.255(255)	2
Bi1	0.75	0.25	0.5	0.917(159)	2
Bi2	0.25	0.25	0.16700(29)	1.027(158)	2
$T = 4$ K					
Symmetry group: $P4/nmm$ Bragg R-factor: 4.83					
$a = b = 4.46(1)$, $c = 10.73(2)$ Magnetic moment $4.3(1)\mu_B$/Mn.					
Atom	x	y	z	B_{iso}	Site multiplicity
Yb1	0.25	0.25	0.73143(21)	0.379(173)	2
Mn1	0.75	0.25	0.0	0.707(272)	2
Bi1	0.75	0.25	0.5	0.188(194)	2
Bi2	0.25	0.25	0.16567(32)	0.256(187)	2

$\eta = 0.00695$ mJ mol^{-1} K^{-6}. Thus, a Debye temperature of 149 K can be obtained.

Clear oscillations in longitudinal ρ_{xx} and transverse ρ_{xy} resistivity are observed up to 35 Tesla [Figs. 3(a)–3(d)]. Whereas the oscillations ρ_{xx} are due to the Shubnikov–de Haas (SdH) effect, the changes of ρ_{xy} with magnetic field could also show a contribution from the quantum Hall effect similar to Bi_2Se_3 due to the layered crystal structure and quasi-2D electronic transport [35]. From the fast Fourier transform (FFT) background-subtracted oscillating component $\Delta\rho_{xx}$ features a single frequency $F = 130$ T at 2 K [Fig. 3(b)]. According to the classical expression for the Hall coefficient

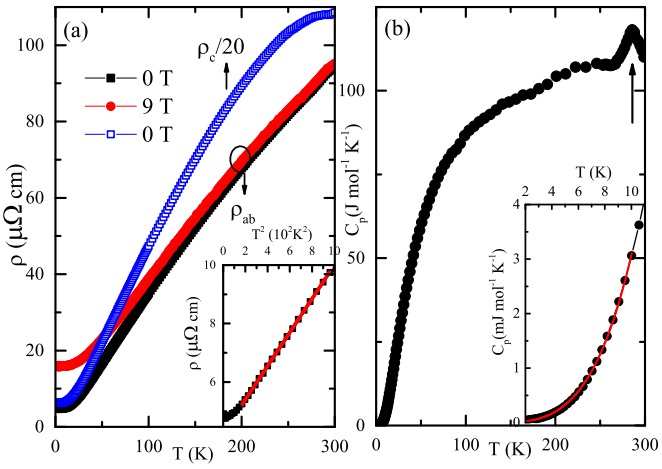

FIG. 2. (a) Temperature dependence of in-plane resistivity (ρ_{ab}) for $YbMnBi_2$ single crystals at 0 and 9 T, and out-of-plane resistivity (ρ_c) at 0 T. Inset shows the quadratic T dependence at low temperature of ρ_{ab} at 0 T. (b) Temperature dependence of the specific heat of $YbMnBi_2$. Inset shows the fitting of the low-temperature part.

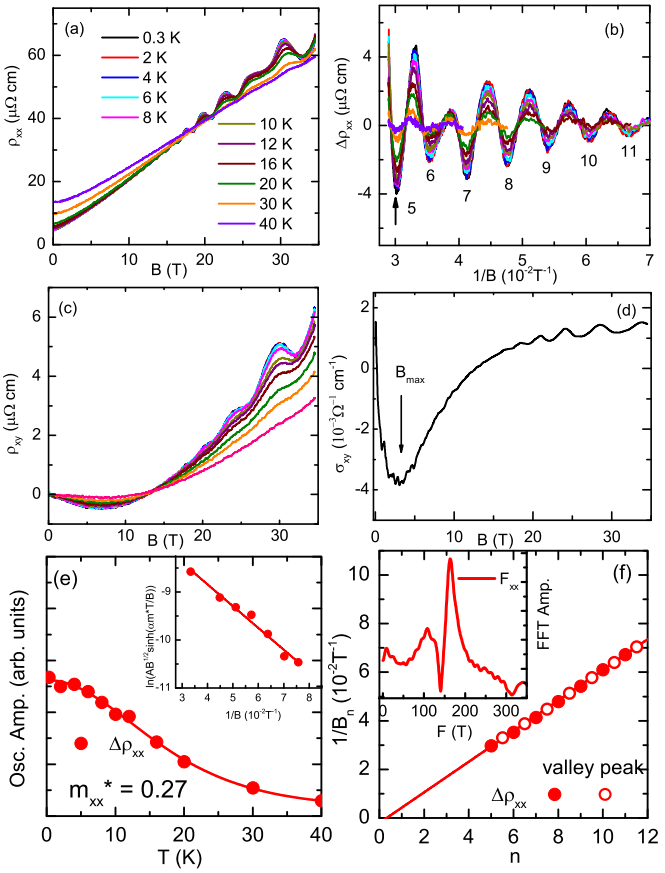

FIG. 3. (a)–(c) Longitudinal and transverse in-plane resistivity vs field at different temperatures. SdH oscillatory component $\Delta\rho_{xx}$. (b) is obtained after the background subtraction. (d) Field dependence of Hall conductivity σ_{xy} at 2 K. (e) Temperature dependence of the oscillating amplitude of longitudinal oscillations at $1/B = 0.33$ T^{-1}. The solid line is the fitting curve. Inset: Dingle plot for $\Delta\rho_{xx}$. (f) LL index plots $1/B_n$ vs n. Inset: The Fourier transform spectrum of $\Delta\rho_{xx}$.

when both electron- and hole-type carriers are present [36], we get

$$\frac{\rho_{xy}}{\mu_0 H} = R_H = \frac{1}{e}\frac{\left(\mu_h^2 n_h - \mu_e^2 n_e\right) + (\mu_h\mu_e)^2(\mu_0 H)^2(n_h - n_e)}{(\mu_e n_h + \mu_h n_e)^2 + (\mu_h\mu_e)^2(\mu_0 H)^2(n_h - n_e)^2}.$$

In the weak-field limit, the equation can be simplified as $R_H = e^{-1}(\mu_h^2 n_h - \mu_e^2 n_e)/(\mu_h n_h + \mu_e n_e)^2$, while $R_H = 1/(n_h - n_e)e$ in the high-field limit. The positive slope of $\rho_{xy}(H)$ at high field gives $n_h > n_e$, and the negative slope of $\rho_{xy}(H)$ at weak field indicates $(\mu_h^2 n_h - \mu_e^2 n_e) < 0$. Therefore, $\mu_e > \mu_h$ at low field, and the nonlinear behavior is the result of the carrier density and mobility competition between hole- and electron-type carriers. Fitting $\rho_{xy}(2K)$ at high field using $R_H = 1/(n_h - n_e)e$ yields $n_h - n_e = 2.09 \times 10^{21}$ cm^{-3}, which is a large carrier concentration when compared to other Weyl semimetals, such as Cd_3As_2 and NbP [27,37].

Theoretical calculations reveal that the Fermi surface of $YbMnBi_2$ is constituted of holelike "lenses" and electronlike pockets near X points [28]. The main frequency of longitudinal

oscillation (130 T) is somewhat smaller than the frequencies of $SrMnBi_2$ (152 T) and $CaMnBi_2$ (185 T) [16,17]. From the Onsager relation, $F = (\Phi_0/2\pi^2)A_F$, where Φ_0 is the flux quantum and A_F is the orthogonal cross-sectional area of the Fermi surface, we estimate $A_F = 1.56\ \mathrm{nm}^{-2}$. This is rather small, similar to that in $SrMnBi_2$ ($1.45\ \mathrm{nm}^{-2}$), and is only a few % of the total area of the Brillouin zone in the (001) plane [16,17]. We can also approximate $k_F \approx 0.705\ \mathrm{nm}^{-1}$, assuming the circular cross section $A_F = \pi k_F^2$.

Weyl points and the Fermi arc connecting these points have been directly observed by angle-resolved photoemission spectroscopy (ARPES) in $YbMnBi_2$ [28]. It is reported that the Fermi arcs, which participate in unusual closed magnetic orbits by traversing the bulk of the sample to connect opposite surfaces, can be detected by quantum oscillation [38]. In our experiment, we do not observe the frequency associated with the Fermi arc, possibly due to macroscopic thickness of our sample that exceeds the mean-free path [38,39].

The cyclotron masses and quantum lifetime of carriers can be extracted from the temperature and field dependence of oscillation amplitude using the Lifshitz-Kosevich formula [40],

$$\frac{\Delta\rho_{xx}(T,B)}{\rho_{xx}(0)} = e^{-\alpha m^* T_D/B}\frac{\alpha m^* T/B}{\sinh(\alpha m^* T/B)},$$

where $\alpha = 2\pi^2 k_\mathrm{B}/\mathrm{e}\hbar \approx 14.69$ T/K, $m^* = m/m_e$ is the cyclotron mass ratio (m_e is the mass of the free electron), and $T_D = \frac{\hbar}{2\pi k_B \tau_q}$, with τ_q the quantum lifetime. By fitting the thermal damping of the oscillation peak indicated by the arrow in Fig. 3(b), we can extract the cyclotron mass $m^* \approx 0.27$, similar to that in $SrMnBi_2$ and $CaMnBi_2$ [15,17]. Then, a very large Fermi velocity $v_F = \hbar k_F/m^* = 3.01 \times 10^5$ m/s can be obtained. As shown in Fig. 3(e), $T_D = 11.4$ K can be obtained by fitting the field dependence of the oscillation amplitude, and T_D is larger than that in $SrMnBi_2$ and $BaMnBi_2$ [17,41]. As a result, $\tau_q = 1.05 \times 10^{-13}$ s. Within the standard Bloch-Boltzmann framework, the geometric mean of the mobility can be determined by the reciprocal value of the peak field, $1/B_{\mathrm{max}}$. As shown in the inset of Fig. 3(c), the geometric-mean mobility $\mu_m = 3.48 \times 10^3\ \mathrm{cm^2\ V^{-1}\ s^{-1}}$ can be inferred from $\mathrm{B_{max}}$ in σ_{xy}. Hence, $\tau_m = 5.3 \times 10^{-13}$ s can be obtained using $\mu_m = e\tau_m/m^*$. This is five times larger than τ_q. This is because τ_m measures backscattering processes that relax the current, while τ_q is sensitive to all processes that broaden the Landau levels [42,43].

Using the effective mass obtained above, we can calculate the electronic specific heat in a quasi-two-dimensional approximation [44],

$$\gamma_N = \sum_i \frac{\pi N_A k_B^2 ab}{3\hbar^2} m^*,$$

where N_A is Avogadro's number, k_B is Boltzmann's constant, a and b are the in-plane lattice parameters, m^* is the quasiparticle mass, and $\hbar$ is Planck's constant. From the effective mass obtained by quantum oscillation, and four bands observed by ARPES [28], $\gamma_N = 2.16\ \mathrm{mJ\ mol^{-1}\ K^{-2}}$ can be obtained, in excellent agreement with the γ_N derived from specific heat [Fig. 2(b)], consistent with ARPES measurement [28] and indicating that four bands detected by SdH alone contribute to the electronic specific heat.

One of the key pieces of evidence for the existence of Dirac fermions is the nontrivial Berry's phase [45]. Figure 3(f) presents the fan diagram of the Landau index. According to the Lifshitz-Onsager quantization rule, LL index n is related to the cross section of the Fermi surface (FS) S_F by $S_F(\hbar/eB) = 2\pi(n+\gamma)$. As shown in Fig. 3(f), the peak and valley positions of ρ_{xx} fall on a straight line; the fit gives $\gamma = 0.21$. γ should be zero for conventional metals, but $(\pm 1/2)$ for Dirac fermions due to the nonzero Berry's phase associated with their cyclotron motion. Berry phase deviations from the exact π value have also been observed in NbP, Bi_2Se_3, and Bi_2Te_2Se [27]. One possible reason behind the deviation is the significant spin-orbit coupling since $\gamma = (1/2) + gm^*/4m$, where g is the g factor, m^* is the cyclotron mass, and m is the electron mass [46–48]. Another possibility is that parabolic bands at the Fermi surface contribute to quantum oscillations and to the high carrier concentration [28].

The Bi square nets in $SrMnBi_2$, and $CaMnBi_2$ host Dirac states with quasi-2D Fermi surface. We perform the field dependence of longitudinal resistance up to 35 T at different angles to study the topological structure of $YbMnBi_2$. The geometry of the measurement setup is shown in the inset of Fig. 4(a). Figure 4(a) presents an angle-dependent oscillation component after background subtraction. The oscillation peaks shift systematically with the angle increase. We perform FFT on the data in Fig. 4(a) and the results are shown in Fig. 4(b). Two peaks can be observed in the low-angle data; we only take the main peak into consideration. The positions of the main peak are summarized in Fig. 4(c); the frequency increases with the angle tilt from zero. The angle dependence of the FFT peaks can be roughly fitted assuming dominant contribution of quasi-2D conducting states $[F(0)/\cos\theta]$ at the Fermi surface. However [Fig. 4(c)], the ellipsoid function $F(0)/(\varepsilon^2\sin^2\theta + \cos^2\theta)^{1/2}$ offers an alternative description. This makes it difficult to distinguish between the 2D cylinder Fermi surface and 3D ellipsoid Fermi surface, but nevertheless a quasi-2D Fermi surface can be inferred. In addition, a dip between -23° to -31° also confirms the nontrivial nature of the $YbMnBi_2$ Fermi surface.

The MR of solids only responds to the extremal cross section of the Fermi surface along the field direction. For a 2D Fermi surface, the MR will only respond to the perpendicular component of the magnetic field $B\cos(\theta)$. The angle-dependent MR of a $YbMnBi_2$ single crystal at $B = 9$ T and $T = 2$ K is shown in Fig. 4(d). The MR shows twofold symmetry; when the magnetic field parallels the c axis of the single crystal ($\theta = 0$), the MR is maximized and it gradually decreases with the field titling away from the c axis. The MR is minimized when the field is applied in the ab plane. The curve can be fitted by a function of $|\cos(\theta)|$, indicating that the quasi-2D Fermi surface dominates magnetotransport in $YbMnBi_2$, consistent with the angle dependence of the quantum oscillation results.

Figure 5(a) presents the magnetic field dependence of MR at different temperatures. MR is also plotted in Fig. 5(b) on a log-log scale to emphasize the low-field behavior. From Fig. 5(b), we can observe that linear MR behavior is established above a crossover field B^*. With increasing temperature, MR gradually decreases and B^* increases. The normal MR of bands with parabolic dispersion either saturates

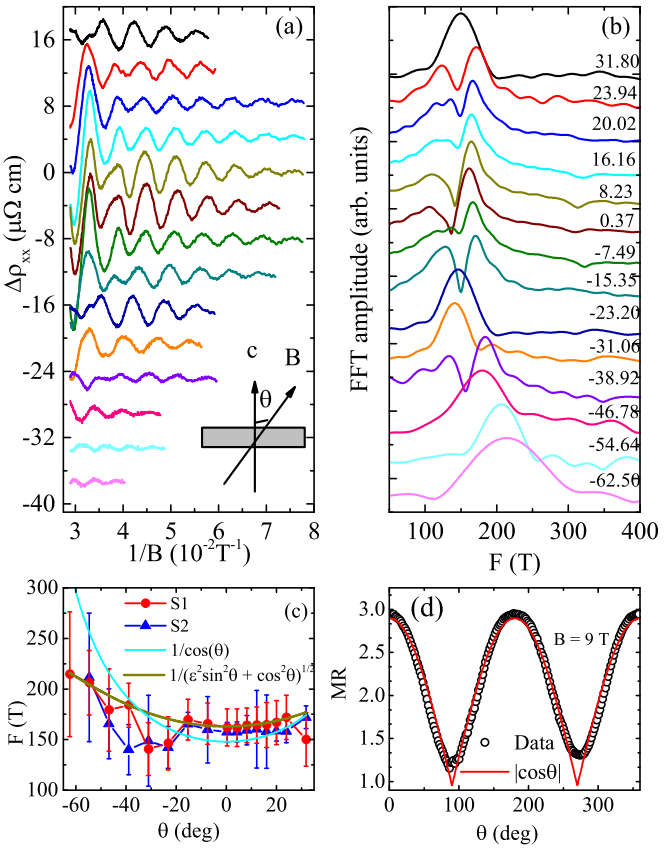

FIG. 4. (a) The SdH oscillatory component as a function of $1/B$ at various angles; the cartoon shows the geometry of the measurement setup. (b) FFT spectra of the SdH oscillations in (a). (a) and (b) use the same legend. (c) Angular dependence of the oscillation frequency. Sample 1 (S1) is the sample we used in this paper; sample 2 is the sample from the same batch and measured on the same probe. The cyan line is the fitting using the 2D model with $F(0)/\cos(\theta)$; the dark yellow line is the ellipse model $F(0)/(\varepsilon^2\sin^2\theta + \cos^2\theta)^{1/2}$ with an anisotropic factor $\varepsilon = -0.67$. The error bar is the peak width at half height of the FFT peaks. (d) Magnetoresistance as a function of the titled angle from the applied field. The red line is the fitting using the 2D model.

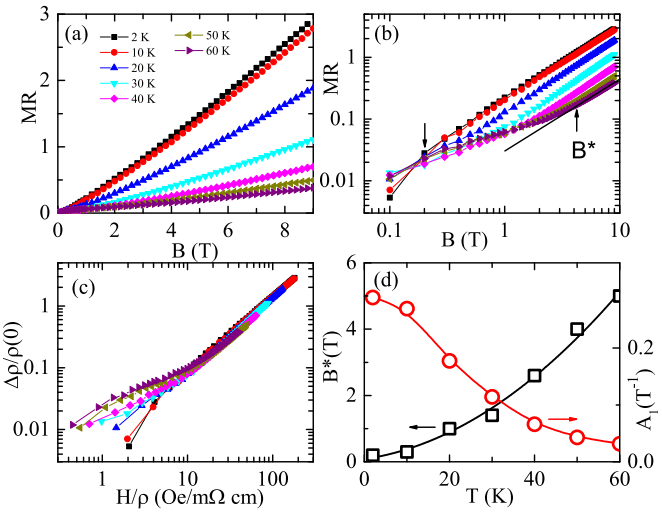

FIG. 5. (a) The magnetic field dependence of the in-plane MR at different temperatures. (b) Log-log plot of MR vs magnetic field. (c) A Kohler plot for $YbMnBi_2$. (d) Temperature dependence of the critical field B^* (black squares); the red solid line is the fitting results using $B^* = (1/2e\hbar v_F^2)(k_BT + E_F)^2$. The red circle corresponds to high-field MR linear coefficient A_1.

at high fields or increases as H^2. The unusual nonsaturating linear magnetoresistance has been reported in $Ag_{2-\delta}(Te/Se)$, Bi_2Te_3,Cd_3As_2, $BaFe_2As_2$, and (Ca, Sr)$MnBi_2$ [15,16]. In the quantum limit where all of the carriers occupy only the lowest LL, the observed B^* corresponds to the quantum limit of $B^* = (1/2e\hbar v_F^2)(k_BT + E_F)^2$ [11]. As shown in Fig. 5(c), the B^* can be fitted quite well by the above equation, which confirms the the existence of Dirac states in $YbMnBi_2$. Furthermore, MR in $YbMnBi_2$ conforms to Kohler's rule, $\Delta\rho/\rho(0) = F[H/\rho(0)]$ [where $F(H)$ usually follows a power law] in high magnetic fields [Fig. 5(c)]. This indicates that there is a single salient scattering time in $YbMnBi_2$, i.e., that even though the Fermi surface contains a contribution from multiple bands, highly conducting (i.e., Dirac) states dominate the MR.

V. CONCLUSIONS

We have demonstrated quantum transport in antiferromagnetically ordered $YbMnBi_2$ single crystals. At 4 K, the saturated magnetic moment is $4.3(1)\mu_B$/Mn, whereas Mn magnetic moments are oriented along the c axis. High-magnetic-field magnetotransport is consistent with the presence of Dirac fermions and significant spin-orbit coupling of the Dirac-like carriers or with the presence of parabolic bands. It would be of interest to study in depth details of the magnetic structure, Berry phase in ultrathin samples, and putative ferromagnetic states in doped crystals.

ACKNOWLEDGMENTS

V.O.G. gratefully acknowledge H. Cao for the support during the neutron diffraction experiment. Work at BNL was supported by the U.S. Department of Energy-BES, Division of Materials Science and Engineering, under Contract No. DE-SC0012704. Work at the National High Magnetic Field Laboratory is supported by the NSF Cooperative Agreement No. DMR-0654118, and by the state of Florida. Work at the Oak Ridge National Laboratory was sponsored by the Scientific User Facilities Division, Office of Basic Energy Sciences, U.S. Department of Energy. X-ray scattering data were collected at the 28-ID-C x-ray powder diffraction beam line at National Synchrotron Light Source II at Brookhaven National Laboratory.

[1] T. O. Wehling, A. M. Black-Schaffer, and A. V. Balatsky, Adv. Phys. **63**, 1 (2014).

[2] O. Vafek and A. Vishwanath, Annu. Rev. Condens. Matter Phys. **5**, 83 (2014).

[3] P. Richard, K. Nakayama, T. Sato, M. Neupane, Y.-M. Xu, J. H. Bowen, G. F. Chen, J. L. Luo, N. L. Wang, X. Dai, Z. Fang, H. Ding, and T. Takahashi, Phys. Rev. Lett. **104**, 137001 (2010).

[4] J. Orenstein and A. J. Millis, Science **288**, 468 (2000).

[5] K. S. Novoselov, A. K. Geim, S. V. Morozov, D. Jiang, M. I. Katsnelson, I. V. Grigorieva, S. V. Dubonos, and A. A. Firsov, Nature (London) **438**, 197 (2005).

[6] A. K. Geim and K. S. Novoselov, Nat. Mater. **6**, 183 (2007).

[7] A. H. Castro Neto, F. Guinea, N. M. R. Reres, K. S. Novoselov, and A. K. Geim, Rev. Mod. Phys. **81**, 109 (2009).

[8] M. Z. Hasan and C. L. Kane, Rev. Mod. Phys. **82**, 3045 (2010).

[9] X. L. Qi and S. C. Zhang, Rev. Mod. Phys. **83**, 1057 (2011).

[10] A. A. Abrikosov, *Fundamentals of the Theory of Metals* (North-Holland, Amsterdam, 1988).

[11] A. A. Abrikosov, Phys. Rev. B **58**, 2788 (1998).

[12] Y. Zhang, Y.-W. Tan, H. L. Stormer, and P. Kim, Nature (London) **438**, 201 (2005).

[13] D. Miller, K. Kubista, G. Rutter, M. Ruan, W. de Heer, P. First, and J. Stroscio, Science **324**, 924 (2009).

[14] K. K. Huynh, Y. Tanabe, and K. Tanigaki, Phys. Rev. Lett. **106**, 217004 (2011).

[15] Kefeng Wang, D. Graf, Hechang Lei, S. W. Tozer, and C. Petrovic, Phys. Rev. B **84**, 220401(R) (2011).

[16] Kefeng Wang, D. Graf, Limin Wang, Hechang Lei, S. W. Tozer, and C. Petrovic, Phys. Rev. B **85**, 041101(R) (2012).

[17] J. Park, G. Lee, F. Wolff-Fabris, Y. Y. Koh, M. J. Eom, Y. K. Kim, M. A. Farhan, Y. J. Jo, C. Kim, J. H. Shim, and J. S. Kim, Phys. Rev. Lett. **107**, 126402 (2011).

[18] L.-L. Jia, Z.-H. Liu, Y.-P. Cai, T. Qian, X.-P. Wang, H. Miao, P. Richard, Y.-G. Zhao, Y. Li, D.-M. Wang, J.-B. He, M. Shi, G.-F. Chen, H. Ding, and S.-C. Wang, Phys. Rev. B **90**, 035133 (2014).

[19] G. Lee, M. A. Farhan, J. S. Kim, and J. H. Shim, Phys. Rev. B **87**, 245104 (2013).

[20] Y. Feng, Z. J. Wang, Ch. Y. Chen, Y. G. Shi, Z. J. Xie, H. M. Yi, A. J. Liang, S. L. He, J. F. He, Y. Y. Peng, X. Liu, Y. Liu, L. Zhao, G. D. Liu, X. L. Dong, J. Zhang, C. T. Chen, Z. Y. Xu, X. Dai, Z. Fang, and X. J. Zhou, Sci. Rep. **4**, 5385 (2014).

[21] Leon Balents, Physics **4**, 36 (2011).

[22] A. A. Burkov, M. D. Hook, and Leon Balents, Phys. Rev. B **84**, 235126 (2011).

[23] X. Wan, A. M. Turner, A. Vishwanath, and S. Y. Savrasov, Phys. Rev. B **83**, 205101 (2011).

[24] S. Y. Xu, C. Liu, S. K. Kushwaha, R. Sankar, J. W. Krizan, I. Belopolski, M. Neupane, G. Bian, N. Alidoust, T.-R. Chang, H.-T. Jeng, C.-Y. Huang, W.-F. Tsai, H. Lin, P. P. Shibayev, F.-C. Chou, R. J. Cava, and M. Z. Hasan, Science **347**, 294 (2015).

[25] S.-Y. Xu, I. Belopolski, D. S. Sanchez, C. Zhang, G. Chang, C. Guo, G. Bian, Z. Yuan, H. Lu, T.-R. Chang, P. P. Shibayev, M. L. Prokopovych, N. Alidoust, H. Zheng, C.-C. Lee, S.-M. Huang, R. Sankar, F. Chou, C.-H. Hsu, H.-T. Jeng, A. Bansil, T. Neupert, V. N. Strocov, H. Lin, S. Jia, and M. Z. Hasan, Sci. Adv. **1**, e1501092 (2015).

[26] S. Y. Xu, N. Alidoust, I. Belopolski, Z. J. Yuan, G. Bian, T.-R. Chang, H. Zheng, V. N. Strocov, D. S. Sanchez, G. Q. Chang, C. L. Zhang, D. X. Mou, Y. Wu, L. N. Huang, C.-C. Lee, S.-M. Huang, B. Wang, A. Bansil, H. Jeng, T. Neupert, A. Kaminski, H. Lin, S. Jia, and Z. Hasan, Nat. Phys. **11**, 748 (2015).

[27] C. Shekhar, A. K. Nayak, Y. Sun, M. Schmidt, M. Nicklas, I. Leermakers, U. Zeitler, Y. Skourski, J. Wosnitza, Z. K. Liu, Y. L. Chen, W. Schnelle, H. Borrmann, Y. Grin, C. Felser, and B. H. Yan, Nat. Phys. **11**, 645 (2015).

[28] S. Borisenko, D. Evtushinsky, Q. Gibson, A. Yaresko, T. Kim, M. N. Ali, B. Buechner, M. Hoesch, and R. J. Cava, arXiv:1507.04847.

[29] A. P. Hammersley, S. O. Swenson, M. Hanfland, and D. Hauseman, High Press. Res. **14**, 235 (1996).

[30] A. C. Larson and R. B. von Dreele, Report No. LAUR-86-748 (Los Alamos National Laboratory, New Mexico, 1987).

[31] B. H. Toby, J. Appl. Crystallogr. **34**, 210 (2001).

[32] D. B. Gutman and D. L. Maslov, Phys. Rev. Lett. **99**, 196602 (2007).

[33] D. B. Gutman and D. L. Maslov, Phys. Rev. B **77**, 035115 (2008).

[34] Y. F. Guo, A. J. Princep, X. Zhang, P. Manuel, D. Khalyavin, I. I. Mazin, Y. G. Shi, and A. T. Boothroyd, Phys. Rev. B **90**, 075120 (2014).

[35] H. Cao, Jifa Tian, I. Miotkowski, Tian Shen, Jiuning Hu, Shan Qiao and Yong P. Chen, Phys. Rev. Lett. **108**, 216803 (2012).

[36] R. A. Smith, *Semiconductors* (Cambridge University Press, Cambridge, 1978).

[37] L. P. He, X. C. Hong, J. K. Dong, J. Pan, Z. Zhang, J. Zhang, and S. Y. Li, Phys. Rev. Lett. **113**, 246402 (2014).

[38] A. C. Potter, I. Kimchi, and A. Vishwanath, Nat. Commun. **5**, 5161 (2014).

[39] P. J. W. Moll, N. L. Nair, T. Helm, A. C. Potter, I. Kimchi, A. Vishwanath, and J. G. Analytis, Nature (London) **535**, 266 (2016).

[40] D. Shoeneberg, *Magnetic Oscillation in Metals* (Cambridge University Press, Cambridge, 1984).

[41] L. J. Li, K. F. Wang, D. Graf, L. M. Wang, A. F. Wang, and C. Petrovic, Phys. Rev. B **93**, 115141 (2016).

[42] T. Liang, Q. Gibson, M. N. Ali, M. H. Liu, R. J. Cava, and N. P. Ong, Nat. Mater. **14**, 280 (2015).

[43] C. L. Zhang, Z. J. Yun, S. Y. Xu, Z. Q. Lin, B. B. Tong, M. Z. Hasan, J. F. Wang, C. Zhang, and S. Jia, arXiv:1502.00251.

[44] N. Kikugawa, A. W. Rost, C. W. Hicks, A. J. Schofield, and A. P. Mackenzie, J. Phys. Soc. Jpn. **79**, 024704 (2010).

[45] Yoichi Ando, J. Phys. Soc. Jpn. **82**, 102001 (2013).

[46] G. P. Mikitik and Yu. V. Sharlai, Phys. Rev. B **67**, 115114 (2003).

[47] G. P. Mikitik and Yu. V. Sharlai, Phys. Rev. B **85**, 033301 (2012).

[48] L. A. Falkovskii, J. Expt. Theor. Phys. **17**, 1302 (1963).